Stress damage process of silicon wafer under millisecond laser irradiation

Zhichao Jia (贾志超)[1], Tingzhong Zhang (张廷忠)[2], Huazhong Zhu (朱华中)[1], Zewen Li (李泽文)[1], Zhonghua Shen (沈中华)[1], Jian Lu (陆 健)[1], and Xiaowu Ni (倪晓武)[1,*]

[1]*School of Science, Nanjing University of Science & Technology, Nanjing 210094, China*
[2]*Institute of Mechanical and Electrical Engineering, Zhoukou Normal University, Zhoukou 466000, China*
**Corresponding author: nxw@njust.edu.cn*

Received September 12, 2017; accepted December 1, 2017; posted online December 27, 2017

The stress damage process of a single crystal silicon wafer under millisecond laser irradiation is studied by experiments and numerical simulations. The formation process of low-quality surface is monitored in real-time. Stress damage can be observed both in laser-on and -off periods. Plastic deformation is responsible for the first stress damage in the laser-on period. The second stress damage in the laser-off period is a combination of plastic deformation and fracture, where the fundamental cause lies in the residual molten silicon in the ablation hole.

OCIS Codes: 140.3330, 140.3390, 160.6000.
doi: 10.3788/COL201816.011404.

Laser drilling is of great importance in modern industry due to its advantages, including low cost, fast speed, and no contact[1]. The studies of laser drilling have been mainly devoted to the femtosecond laser and nanosecond laser, and very few studies relate to the millisecond laser. This is because the processing quality induced by the short-pulse laser is much higher than by the millisecond laser[2–4]. However, the laser energy is easily shielded and wasted due to air breakdown and plasma[5,6]. The millisecond laser has some distinctive features: larger pulse energy and high efficiency of energy coupling. The processing quality may be improved if the interaction mechanisms can be comprehensively understood. Previous investigations of millisecond laser drilling have focused primarily on metallic materials. In these cases, melting and ablation are the main damage mechanisms. The processing quality is mainly described by the keyhole[7,8]. If the drilling process is performed in silicon, stress damage becomes another important damage mechanism, which greatly reduces processing quality.

In order to analyze the damage process, both experimental and numerical methods have been widely used. Li *et al.* had given time-resolved surface temperature of millisecond laser irradiated silicon to study the temperature field. The heating process can be well described by a finite element model[9]. Wang *et al.* had investigated the thermal stress using an axisymmetric model, where the crystal silicon was treated as isotropic material. The crack distribution was also investigated[10]. Choi *et al.* built a more complex three-dimensional model and took the crystal structure into account[11]. Their analyses are all based on the final damage morphology, which is observed after the experiment, and are not comprehensive due to the neglected dynamic ablation process. Real-time monitoring is a direct way to observe the dynamic damage process. In this Letter, the dynamic formation process of the low-quality surface is investigated by real-time monitoring. It is more thorough in understanding the damage process by combining the experimental results and the numerical analysis.

The experimental setup is schematically shown in Fig. 1. The 1080 nm irradiation laser operating at the transverse electromagnetic (TEM_{00}) mode is normally incident onto the front surface of the {001} silicon wafer. The beam size ($1/e^2$ radius) at the surface is about 1 mm, and the pulse width is 1 ms. The sample used is a single crystal silicon wafer with the front surface mirror polished, and the thickness is ~300 μm. The probe beam from a continuous semiconductor laser is obliquely projected to the irradiated zone, and the reflected light is recorded with a CCD system. The optical distribution contains the changing information of the irradiated zone. The CCD (exposure time of 10 μs and sampling interval time of 2 ms) takes the first image at 1 ms, and the total record time is 1 s.

The series of representative patterns are shown in Figs. 2 and 3. The processes can be divided into two cases:

Case 1: the laser energy density ranges from 0 to 23 J/cm^2, as shown in Fig. 2. Images are taken at 1 ms when the laser irradiation ends. These patterns remain unchanged in the laser-off period. No damage is found when the laser energy density is lower than 19 J/cm^2. The dark

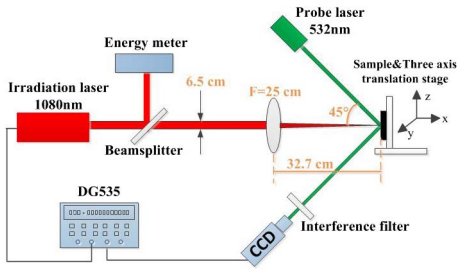

Fig. 1. Experimental setup for testing damage.

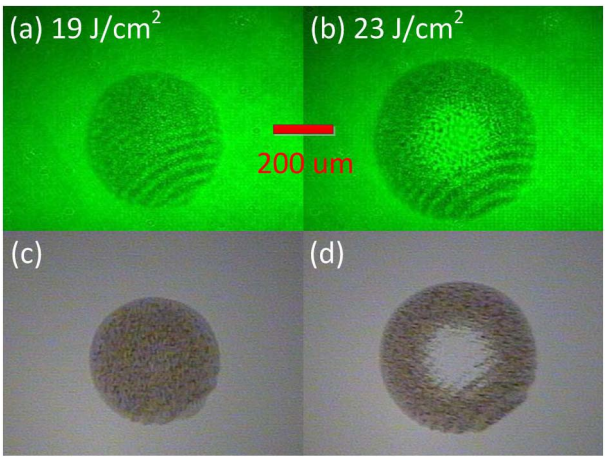

Fig. 2. Real-time images induced by different laser energy densities for (a) 19 and (b) 23 J/cm^2, respectively. (c) and (d) Corresponding morphological images taken by an optical microscope (OM) after experiment.

spot, as shown in Fig. 2(a), is the first damage. When the laser energy density is larger than 23 J/cm^2, the spot center melts and becomes smooth. In fact, stress damage prior to melting is responsible for the dark spot.

Case 2: the laser energy density is far above the melt threshold, as shown in Fig. 3. When the pulse ends, the spot center has melted and become smooth. The outer dark ring indicates the stress damage region. After lasting for a period (~300 ms), another dark spot could be observed in the center [Fig. 3(b)]. Afterward, the dark spot becomes much larger. The flat region outside the dark ring also becomes uneven [Fig. 3(c)]. In the end, cracks are observed [Fig. 4(d)]. Some fragments flake off the cracks. The whole damage process lasts for ~735 ms, which is far longer than the pulse width.

To get further knowledge of the experiment results, the thermal process of the millisecond laser irradiated silicon is numerically calculated by the finite element method. The incident laser beam has a Gaussian shape with a radius of 1 mm. The silicon wafer is 6 mm in radius and 0.3 mm in thickness.

The temperature is obtained by solving the thermal conduction equation:

$$\rho c \frac{\partial}{\mathrm{d}t} T + \nabla \cdot (kT) = Q, \tag{1}$$

where ρ, c, and k are the density, specific heat, and thermal conductivity, respectively. Q is the laser heat source, which can be described by

$$Q = \alpha P(1-R)\exp\left(-2\frac{x^2+y^2}{w_0^2}\right)\exp(-\alpha z), \tag{2}$$

where P is the laser peak power density at the spot center, R and α are the surface reflectivity and the optical absorption coefficient, respectively.

The equivalent specific heat capacity is used to deal with latent heat due to phase transitions: $C_{p,\mathrm{eff}} = C_p + L_m D_m$, where L_m is latent heat of fusion, $D_m = \frac{\exp[(T-T_m)^2/\Delta T_m)^2]}{\sqrt{\pi}\Delta T_m}$ is a pulse function located at melting point T_m, and pulse width ΔT_m is set to 10 K.

For the boundary condition, heat loss caused by convection and surface to ambient radiation are considered:

$$-k\nabla T = h(T_0 - T) + \varepsilon\sigma(T_0^4 - T^4), \tag{3}$$

where h is the heat transfer coefficient, ε is the surface emissivity, and σ is the Stefan–Boltzmann constant.

In (001) silicon with three axes at [100], [010], and [001], the relationship between strain and stress can be expressed as

$$\begin{bmatrix} \varepsilon_x - \alpha_T \Delta T \\ \varepsilon_y - \alpha_T \Delta T \\ \varepsilon_z - \alpha_T \Delta T \\ 2\gamma_{yz} \\ 2\gamma_{xz} \\ 2\gamma_{xy} \end{bmatrix} = \begin{bmatrix} \frac{1}{E} & -\frac{\nu}{E} & -\frac{\nu}{E} & 0 & 0 & 0 \\ -\frac{\nu}{E} & \frac{1}{E} & -\frac{\nu}{E} & 0 & 0 & 0 \\ -\frac{\nu}{E} & -\frac{\nu}{E} & \frac{1}{E} & 0 & 0 & 0 \\ 0 & 0 & 0 & G & 0 & 0 \\ 0 & 0 & 0 & 0 & G & 0 \\ 0 & 0 & 0 & 0 & 0 & G \end{bmatrix} \begin{bmatrix} \sigma_x \\ \sigma_y \\ \sigma_z \\ \tau_{yz} \\ \tau_{xz} \\ \tau_{xy} \end{bmatrix}, \tag{4}$$

where $\{\tau\}^T = [\sigma_x, \sigma_y, \sigma_z, \tau_{xy}, \tau_{yz}, \tau_{zz}]$ is the stress tensor, and $\{\varepsilon\}^T = [\varepsilon_x, \varepsilon_y, \varepsilon_z, \gamma_{xy}, \gamma_{yz}, \gamma_{zz}]$ is the strain tensor. α_T is the thermal expansion coefficient, and ΔT is the temperature rise. E, G, and ν represent Young's modulus, shear modulus, and Poisson's ratio, respectively. E is assumed to be 1×10^6 in liquid silicon (~1×10^{11} in solid state) to describe the stress release caused by phase transition. The physical properties of silicon used in the simulation can be found in our previous work[10,12].

The laser energy density is set to 28 J/cm^2 to get a comparison with the experiment in Fig. 3. The simplest description of the damage process will be made in this

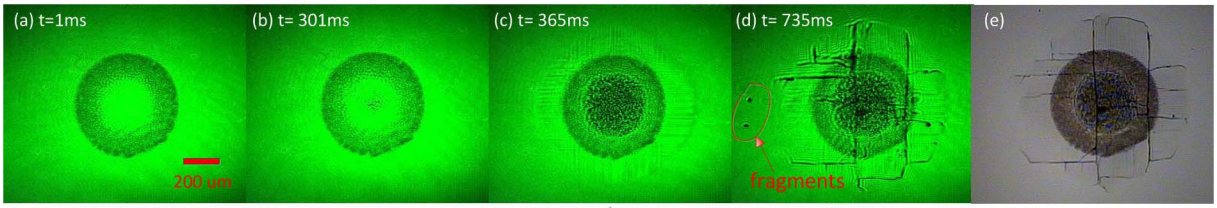

Fig. 3. (a)–(d) Real-time images at different times. The laser energy density is 28 J/cm^2. (e) the morphological image taken by the OM after the experiment.

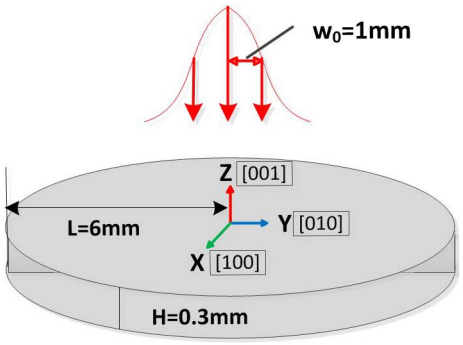

Fig. 4. Simulation model of a silicon wafer under laser irradiation.

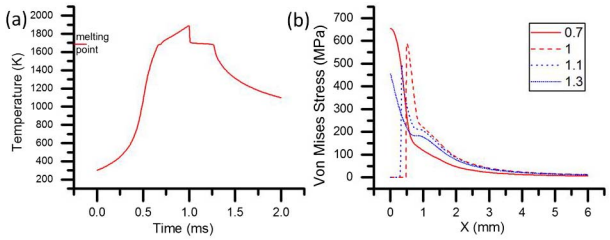

Fig. 5. (Color online) (a) Temperature of spot center and (b) von Mises stresses along the X axis at 0.7, 1, 1.1, and 1.3 ms, respectively.

paragraph. Figure 5(a) shows the temperature of the spot center and von Mises stress along the X axis. The temperature and thermal stress keep increasing until melting occurs. The thermal stress sharply drops to zero when melting occurs. The highest temperature in the spot center has reached 1900 K, which is lower than the vaporization point (3538 K), so the molten liquid will not be squeezed out by recoil pressure. After 1 ms irradiation, the liquid silicon cools rapidly to the melting point and releases latent heat, while the temperature maintains at 1685 K, and a liquid–solid phase change plateau is formed. This phase-transition time is ∼0.3 ms, which is far less than the experimental result (∼300 ms). The difference is caused by stress damage prior to melting. The crystal structure is damaged by thermal stress first, so the absorption of the laser becomes larger than that of ideal crystal. The molten pool at 1 ms should be larger than the result from simulation. Therefore, a longer solidification process is formed. When liquid silicon solidifies to a solid state, stress appears again and releases gradually.

A more accurate description of stress damage should consider both the temperature-dependent properties and the crystal structure of silicon. Silicon is a brittle material at room temperature, which means that its behavior is purely elastic until it fails. When laser heating begins, the spot center has the highest thermal stress. If the stress exceeds yield strength, the crystal structure will be destroyed. When the spot center reaches T_{bd} (∼800 K), the maximum thermal strain is $\varepsilon_{\max} = \int_{293}^{800} \alpha_T \mathrm{d}T \approx 1.3 \times 10^{-3}$, and the maximum thermal stress is $\tau = E_{110}\varepsilon_{\max} \approx 220$ MPa. The yield strength of dislocation-free silicon is ∼3.8 GPa[13]. Therefore, a fracture will not happen in this process. Silicon exhibits a plastic behavior above T_{bd}. The microscopic fracture studies have shown that there is hardly any dislocation below the T_{bd} and a huge number of dislocations above T_{bd}. Then, the transition phenomenon can be explained as a shift in the mechanism from the breaking of covalent bonds between atoms to multiplication and propagation of dislocations[14]. In other words, the stress damage above T_{bd} behaves as plasticity. Slip is the main mechanism of plastic deformation in crystal silicon. The question whether slip happens before melting has been solved by comparing the resolved shear stress and the yield strength of possible slip systems. It has been demonstrated that slip always takes place prior to melting when silicon is under millisecond laser irradiation, so the dark spot in real-time images means the plastic region[15]. The plastic region has no obvious anisotropic characteristic, although slip is directional. This is caused by the approximately isotropic motion of dislocations for there are at least 12 possible slip systems.

When melting occurs, thermal stress decreases, and the plastic region stops enlarging. When molten liquid solidifies, the spot center still has the largest thermal stress, and plastic deformation takes place again. The new plastic region enlarges and eventually reaches the old plastic ring, as shown in Fig. 3(c). Then, the surface morphology stays unchanged for ∼300 ms until fracture happens. The unchanged morphology in this process can be explained as a shift of stress releasing mechanism from dislocation propagation to dislocation block. The temperature on the front surface decreases from the spot center radially. In the high temperature region, dislocation multiplication and propagation make the plastic region enlarge, while in the low temperature region, dislocation is hard to move due to its strong temperature dependence. The dislocation block is responsible for not only the area of the plastic region but also subsequent fracture. As discussed above, during the heating process, the thermal stress is too low to introduce fracture. However, during the cooling process, the dislocation block makes the stress concentration at the rim of plastic region[16]. On the other hand, the introduction of plasticity greatly reduces fracture strength. When the temperature decreases below T_{bd}, fracturing happens. This process is evidenced by real-time monitoring. Figure 6 shows the images just before fracturing happens. The central area stays unchanged, while the difference is found in the dashed frame. A vague shape of cracks is formed in Fig. 6(b), and it develops into cracks

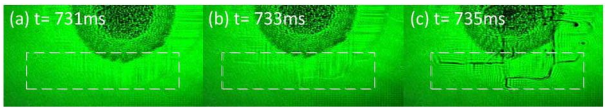

Fig. 6. Images just before fracture. The experiment is the same as that of Fig. 3.

in 2 ms. The observation shows that stress is always releasing through plastic deformation before fracturing happens

The position of the fracture is also interesting due to unique stress distribution. In the experiment, the radius of the plastic region is ~0.5 mm (half of the beam radius). So, an analysis will be made based on the concentric circle, as shown in Fig. 7(a). The concentric circle has the same temperature and yield strength but different resolved shear stress. The resolved shear stresses along the concentric circle at 1.5 ms are shown in Fig. 7(b). With cubic symmetry, we can only consider 3 slip systems: (111)[110], (111)[101], and (111)[011][17]. The maximum shear stress is not in the <110> directions. The deflection angle is ~25°. Once a fracture occurs, cracks tend to maintain on its original planes. Therefore, cracks do not pass through the spot center, as shown in Fig. 3(e). The linear cracks can also turn into circular cracks at the rim of the plastic region because the fracture strengths are much lower in the plastic region than in the ideal region.

Once vaporization occurs, the molten liquid will be squeezed out. As shown in Fig. 8(a), although an ablation hole has been formed, cracks are also introduced during the cooling process. Some of the molten liquid is squeezed from the molten pool and deposits at the periphery, which corresponds to the white ring around the ablation hole. The thickness of the molten liquid layer is ~100 μm, which is comparable to the thickness of the silicon wafer (300 μm). So, the solidification process of molten liquid has great influence on the substrate.

The thinner the molten layer, the less there is an effect on the substrate. During the ablation process, the laser energy is mainly absorbed by the surface layer of molten liquid, and then it is free to diffuse to greater depths via thermal conduction. Therefore, the thermal diffusion length plays an important role in the thickness of molten liquid. For the millisecond laser, the thermal diffusion length is ~250 μm, while for the nanosecond laser, the thermal diffusion length can be reduced to ~10 μm[18]. Then, the effect of the molten layer on the substrate can be reduced to the least extent. Figure 8(b) shows the surface morphology induced by a nanosecond laser. The damage morphology characteristic is surface layer damage. The molten liquid solidified at the rim of the ablation hole, and no crack is observed.

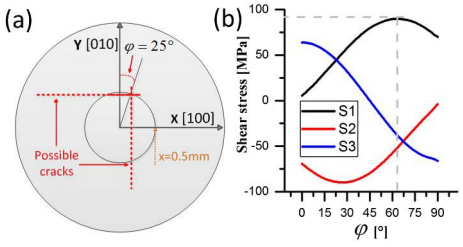

Fig. 7. (Color online) (a) Concentric circle and (b) shear stresses along it at 1.5 ms. S1, S2, and S3 represent the shear stress along (111)[110], (111)[101], and (111)[011], respectively.

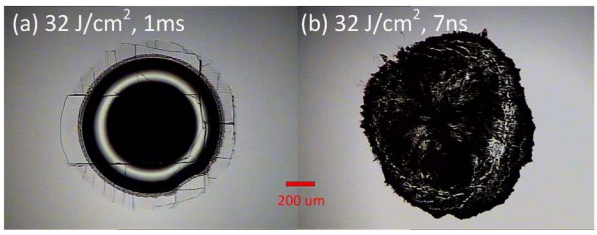

Fig. 8. (a) Typical ablation morphology induced by a millisecond laser and (b) a nanosecond laser.

In conclusion, the damage process of a single crystal silicon wafer under millisecond laser ablation is studied by experiments and numerical simulations. Stress damage happens both in the laser-on period and laser-off period. In the laser-on period, plastic deformation happens first, and the plastic region is larger than the ablation hole. In the laser-off period, the solidification of molten liquid causes a second stress damage, which is more serious than the previous one. The second stress damage is caused by thick molten liquid and seems possible to avoid by removal of the molten liquid. However, the first plasticity can be suppressed only when the laser pulse is less than ~14 μs[15]. So, it is very promising to combine two different pulses to improve processing quality and efficiency. The research provides a better understanding of the formation process of low-quality surfaces under millisecond laser ablation and it offers theoretical and experimental basis for further application of the millisecond laser.

This work was supported by the National Natural Science Foundation of China (No. 61605079) and the Fundamental Research Funds for the Central Universities (No. 30916014112-020).

References

1. C. Xu, L. Jiang, N. Leng, Y. Yuan, P. Liu, C. Wang, and Y. Lu, Chin. Opt. Lett. **11**, 041403 (2013).
2. X. Wang, D. H. Zhu, Z. H. Shen, J. Lu, and X. W. Ni, Appl. Surf. Sci. **257**, 1583 (2010).
3. Y. Zhou, B. X. Wu, S. Tao, A. Forsman, and Y. B. Gao, Appl. Surf. Sci. **257**, 2886 (2011).
4. Z. Wu, N. Zhang, M. Wang, and X. Zhu, Chin. Opt. Lett. **9**, 093201 (2011).
5. Y. Liu, Y. Tong, S. Li, Y. Wang, A. Chen, and M. Jin, Chin. Opt. Lett. **14**, 123001 (2016).
6. Q. Wang, Y. Zhang, Z. Wang, J. Ding, Z. Liu, and B. Hu, Chin. Opt. Lett. **14**, 110201 (2016).
7. Y. M. Zhang, Z. H. Shen, and X. W. Ni, Int. J. Heat Mass Transfer **73**, 429 (2014).
8. T. Zhang, X. Ni, and J. Lu, Chin. Opt. Lett. **13**, 081403 (2015).
9. Z. W. Li, H. C. Zhang, Z. H. Shen, and X. W. Ni, J. Appl. Phys. **114**, 033104 (2013).
10. X. Wang, Y. Qin, B. Wang, L. Zhang, Z. H. Shen, J. Lu, and X. W. Ni, Appl. Opt. **50**, 3725 (2011).
11. S. Choi and K.-Y. Jhang, Appl. Phys. Lett. **104**, 251604 (2014).
12. Z. C. Jia, Z. W. Li, X. M. Lv, and X. W. Ni, Appl. Opt. **56**, 4900 (2017).

13. F. W. DelRio, R. F. Cook, and B. L. Boyce, Appl. Phys. Rev. **2**, 021303 (2015).
14. A. Masolin, P.-O. Bouchard, R. Martini, and M. Bernacki, J. Mater. Sci. **48**, 979 (2013).
15. Z. Jia, Z. Li, X. Lv, and X. Ni, Appl. Opt. **56**, 4900 (2017).
16. L. Y. Guo, Z. Chen, J. Long, and T. Yang, Acta Phys. Sin. **64**, 0178102 (2015).
17. S. Choi and K. Y. Jhang, Opt. Eng. **53**, 017103 (2014).
18. X. Wang, Z. H. Shen, J. Lu, and X. W. Ni, J. Appl. Phys. **108**, 033103 (2010).